

# A deep H $\alpha$ survey of the Milky Way

## VI. The $l = 332^\circ$ area<sup>\*,\*\*</sup>

D. Russeil<sup>1</sup>, C. Adami<sup>1</sup>, P. Amram<sup>1</sup>, E. Le Coarer<sup>2</sup>, Y. M. Georgelin<sup>1</sup>, M. Marcelin<sup>1</sup>, and Q. Parker<sup>3</sup>

<sup>1</sup> LAM, 2 Place Le Verrier, 13248 Marseille Cedex 04, France  
e-mail: delphine.russeil@oamp.fr

<sup>2</sup> Observatoire de Grenoble, BP 53X, Grenoble Cedex, France

<sup>3</sup> Department of Physics, Macquarie University, NSW 2109, Australia; Anglo-Australian Observatory, PO Box 296, Epping NSW 1710, Australia

Received 15 April 2004 / Accepted 3 Septembre 2004

**Abstract.** The Galactic plane has been observed between  $l = 330^\circ$  to  $l = 336^\circ$  as part of a velocity resolved H $\alpha$  survey of the southern Milky Way using a scanning Fabry-Perot on a 36 cm telescope. The detailed analysis of the resultant H $\alpha$  profiles reveals the presence of several layers of ionized gas with different velocities over the surveyed region. We have studied in detail both the 2-D spatial and velocity structure of the HII regions RCW102, RCW104 and RCW106. Combining these H $\alpha$  observations with stellar and radio data we provide estimates for the most probable distances of these different layers. The first layer at  $-5 \text{ km s}^{-1}$  is local emission linked to the Sco-Cen association at 170 pc. The next layer, around  $-24 \text{ km s}^{-1}$ , is at 1.9 kpc and traces the near section of the Sagittarius-Carina arm. Well connected to the Sagittarius-Carina arm portions traced in the adjacent regions ( $l = 328^\circ$  and  $l = 338^\circ$  area), the arm, in this longitude range, clearly shows and confirms the departure from a logarithmic spiral. The Scutum-Crux arm is also traced in this area by faint and diffuse emission at  $-40 \text{ km s}^{-1}$  which can be placed at 3.2 kpc. The layer at  $-52 \text{ km s}^{-1}$  is the major spiral-arm feature of the studied area; its most probable stellar distance is 4.2 kpc. An important emission component is also observed at  $-65 \text{ km s}^{-1}$  in the southern part of the surveyed area. This mainly patchy and filamentary emission we identify as the possible optical counterpart of a supernovae remnant centered at  $l = 332.0^\circ$ ,  $b = -3.2^\circ$ . Finally, two complexes have been determined around 12.5 kpc which places them in the far section of the Norma arm.

**Key words.** ISM: HII regions – Galaxy: structure – ISM: kinematics and dynamics

## 1. Introduction

In order to trace the spiral structure of our Galaxy we need to accurately identify and spatially locate the star-forming complexes within the various spiral arms. Each complex can be seen as a giant parental molecular cloud with associated ionized hydrogen, young stars and young clusters. The detailed analysis of the ionized gas (from diffuse emission as well as discrete HII regions) as indicated by the H $\alpha$  line over a range of velocities is essential to associate the observed radio sources with their parental molecular cloud. This is accomplished using their respective velocity and spatial similarity, which can also reveal their possible expansion and internal motions.

In parallel, the exciting stars within this ionized gas make the link between the velocities of these complexes and stellar distance. To address these issues we have been undertaking a long-term targetted H $\alpha$  survey of the southern Milky Way with a 36 cm telescope in La Silla equipped with a scanning

Fabry-Perot and a photon counting camera (Amram et al. 1991; le Coarer et al. 1992). Coupled with multiwavelength data, this survey has led to the compilation of a comprehensive catalogue of star-forming regions enabling us to map these complexes in 3-D. This has enabled us to better delineate the 4-arm spiral model of our Galaxy (Russeil 2003), first postulated by Georgelin & Georgelin (1976).

In terms of galactic significance the  $l = 332^\circ$  direction intersects 3 spiral arms: the Sagittarius-Carina arm, the Scutum-Crux arm and the Norma arm (see Fig. 5 in Russeil 2003). Furthermore this is without pointing in any tangent direction to an arm, thus alleviating possible line of site confusion. It is thus a key area in distinguishing the different spiral arms of the Galaxy and in clarifying the intricate situation seen in the  $l = 338^\circ$  area (Georgelin et al. 1996) and in connecting the  $l = 338^\circ$  and  $l = 328^\circ$  (Georgelin et al. 1994) directions.

The  $l = 328^\circ$  direction revealed the Sagittarius-Carina arm with diffuse emission at 1 kpc from the Sun and with a velocity around  $-20 \text{ km s}^{-1}$ . Another layer with velocity  $-40 \text{ km s}^{-1}$  at 2.3 kpc is detected in front of the Scutum-Crux arm located at  $\sim 3$  kpc with velocity  $-50 \text{ km s}^{-1}$ . Finally, three radio complexes around 7 kpc (velocity between  $-90$  and  $-100 \text{ km s}^{-1}$ )

\* Based on observations collected at the European Southern Observatory.

\*\* Table 1 is only available in electronic form at <http://www.edpsciences.org>

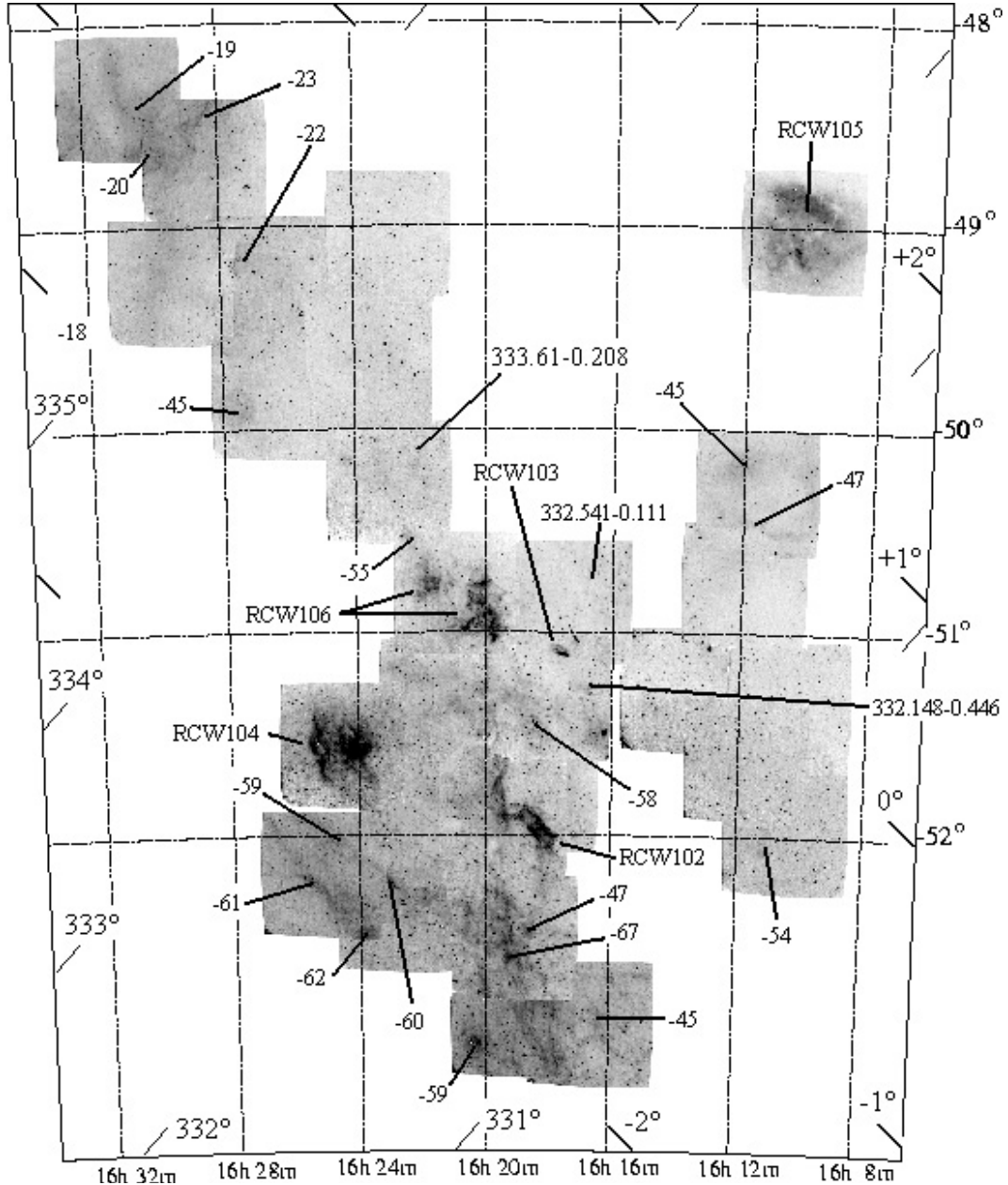


**Fig. 1.** Mosaic of the observed fields. Each image is obtained by adding  $\lambda$  maps over the free spectral range, then flat-fielded and corrected for distortion. It is equivalent to a photograph obtained through a 2.4 Å bandwidth filter. The  $V_{\text{lsr}}$  (km s $^{-1}$ ) of some remarkable H $\alpha$  features and identification of optically detected HII regions are indicated. Coordinates are J2000.

are found near the tangent point of the Norma arm. The  $l = 338^\circ$  direction revealed the presence of 5 optical layers which are quite difficult to clearly place in a spiral arm design. These layers are located at about 1.2 kpc, 2.3 kpc (Sagittarius-Carina arm), 3.1 kpc, 4.4 kpc and 5 kpc. In addition, complexes detected only in radio around 12 and 15 kpc trace the far section of the Norma and Scutum-Crux arms.

The specific area of the galactic plane studied in this paper is at  $l = 330^\circ$  to  $336^\circ$  and  $b = 1.5^\circ$  to  $-2^\circ$ . The observations are described in Sect. 2. Section 3 is devoted to the presentation of the results. Section 4 briefly summarizes the stellar data before a short discussion of the key results (Sect. 5) while conclusions are given in Sect. 6.

## 2. Observations

Data cubes ( $x, y, \lambda$ ) have been obtained (spatial resolution  $9'' \times 9''$ ) for 26 fields ( $38' \times 38'$  each) in the direction around  $332^\circ$  of longitude and  $0^\circ$  of latitude. Figure 1 shows the mosaic of observed fields. A complete description of our instrument, including data acquisition and reduction techniques, has been given in le Coarer et al. (1992). Two different Fabry-Perot interferometers (interference orders  $P = 2604$  or  $P = 796$ , at H $\alpha$  wavelength) were used depending on the anticipated velocity range covered by the observed structures. The interferometers provide a spectral sampling of 5 km s $^{-1}$  and 16 km s $^{-1}$  for a spectral range of 115 km s $^{-1}$  and 376 km s $^{-1}$  respectively. The interference filter used is centered at 6562 Å with a *FWHM* 11 Å.

The majority of fields were observed with the highest order interferometer. Data reduction follows the procedures described in Georgelin et al. (1994). The night-sky lines (geocoronal H $\alpha$  and OH) are modelled by the instrumental function, the nebular lines being modelled by Gaussian profiles convolved with the instrumental function.

The main problem was to provide clear separation between the various faint intensity components found in the complex observed H $\alpha$  line profile. Inside a given field we can distinguish 3 or even 4 main components (not including the geocoronal H $\alpha$  and OH nightsky lines) with each corresponding to a different layer of ionized hydrogen. Generally the different components exhibit the same velocity all over the observed field, which enables us to follow them rather easily despite their highly varying intensity.

### 3. Results

In Table 1 we give the radial velocities ( $V_{\text{lsr}}$ ) of the HII regions found between  $l = 330.5^\circ$  and  $l = 336^\circ$ . They have been grouped according to their velocity and spatial location to permit identification of the large, physically separated complexes.

- Column 1: Source Identification.
- Column 2: H $\alpha$  velocity ( $V_{\text{lsr}}$  from our Fabry-Perot measurements) or H $\alpha$  detection from the UKST plates (AAO/UKST H $\alpha$  survey of the galactic plane, Parker & Phillipps 2003).
- Column 3: Radio recombination velocities from the literature (Caswell & Haynes 1987; Shaver et al. 1983; Paladini et al. 2003).
- Column 4: Molecular (CO and/or CS) velocities from the literature (Brand et al. 1984; Bronfman 2000; Russeil & Castets 2004).
- Column 5: Velocities (from the literature) of absorption lines at H $_2$ CO, OH and HI wavelengths (Caswell & Haynes 1987; Gardner & Whiteoack 1984; Turner 1979; Whiteoack & Gardner 1974).
- Column 6: Adopted systemic velocity of the group and near/far distance choice.
- Column 7: Adopted distance for the complex: either kinematic or stellar distance (stellar distances are indicated by a star symbol before the value).

#### 3.1. Diffuse ionized hydrogen

As we can see from the mosaic (Fig. 1), the North East surveyed region is relatively free of discrete HII regions. Here the determination of diffuse H $\alpha$  emission is easier and three components are seen with mean velocity  $-5$ ,  $-22$  and  $-42$  km s $^{-1}$  respectively.

Averaged throughout the entire mosaic the mean velocity of the first diffuse component is  $-6$  km s $^{-1}$ . This is a local component already detected in many of the other zones of the H $\alpha$  survey. Otrupcek et al. (2000) show that dark-clouds are characterised by CO antenna temperatures between 4.4 to 10.2 K and a linewidth between 1.1 to 2.0 km s $^{-1}$ . We note from Otrupcek's catalogue that between  $l = 330.5^\circ$  and  $335.5^\circ$  the mean  $V_{\text{lsr}}$  of

dark clouds is  $-4.9$  km s $^{-1}$  in good agreement with our diffuse H $\alpha$  measurement, thus underlining their kinematic association.

The second H $\alpha$  diffuse component yields a mean velocity of  $-24$  km s $^{-1}$  (between  $-17.5$  and  $-28.4$  km s $^{-1}$ ) with essentially constant intensity ( $\sim 0.7$  evt./px/h) throughout the surveyed area, except around RCW105 where it reaches 8 evt./px/h. This component is also detected over the whole observed mosaic. Furthermore its presence can also be inferred from the absorption lines noted towards the different radio sources detected (Table 1). Also, from the longitude-velocity maps of Bronfman et al. (1989), we can see a CO cloud with velocity  $-15$  km s $^{-1}$  lying between  $l = 333.25^\circ$  and  $335^\circ$  and  $b = -1.25^\circ$  and  $0.5^\circ$  which can explain the  $-17.5$  km s $^{-1}$  H $\alpha$  velocity.

Finally, two other components are noted around  $-42$  km s $^{-1}$  ( $-36$  to  $-47$  km s $^{-1}$ ) and  $-59$  km s $^{-1}$  ( $-50$  to  $-64$  km s $^{-1}$ ). The  $-42$  km s $^{-1}$  component, detected as diffuse emission in the north of the mosaic, appears more patchy and filamentary in the south. Its intensity range is from 0.3 to 3.7 evt./px/h. The  $-59$  km s $^{-1}$  component is not present in the north and appears exclusively as filaments in the south. Its intensity range is from 0.5 to 8 evt./px/h. Most of the filaments belong to the second velocity group while few belong to the first group, but with both coexisting in some fields. In addition, the analysis of absorption and CO information (Table 1) often shows the presence and/or coexistence of lines at these two velocities.

#### 3.2. RCW105/GUM 51

RCW105 (G333.04+2.02) is a large HII region of strong intensity (from 17 to 70 evt./px/h) and slight internal motions: the southern part exhibits a velocity slightly more negative ( $-23$  km s $^{-1}$ ) than the northern part ( $-19$  km s $^{-1}$ ), while its brightest part exhibits a velocity of  $-26$  km s $^{-1}$ . To determine its systemic velocity we took the mean velocity of the edges to be more significant than those from the possibly kinematically active center. On this basis we assign a velocity of  $-21.3$  km s $^{-1}$  to RCW105. In the direction of RCW105, Yamaguchi et al. (1999) detect two molecular clouds with similar velocity:  $333.3+2.0$  ( $-24.3$  km s $^{-1}$ ) and  $332.4+2.5$  ( $-23.2$  km s $^{-1}$ ). The velocity of the  $-24$  km s $^{-1}$  diffuse component is in very good agreement with the RCW105 velocity making their association undoubted.

In parallel, we searched alternative optical data for an exciting star for RCW105 in order to determine its stellar distance. On the basis of the direction indicated by the associated "elephant trunks" seen on the AAO/UKST H $\alpha$  survey image of the region (survey field HA348, exposure HA18057) we selected two possible exciting stars: HD 144900 (O9III) and HD 144918 (O7V). Note the AAO/UKST H $\alpha$  survey is now available on-line as full resolution 0.6 arcsec pixel data at <http://www-wfau.roe.ac.uk/sss>. From the available photometric information we determined the distance of HD 144900 ( $d = 1.86$  kpc,  $A_v = 3.33$  mag) and HD 144918 ( $d = 1.98$  kpc,  $A_v = 3.49$  mag). Hence the mean stellar distance is 1.9 kpc. This is in very good agreement with the RCW105 kinematic distance (2 kpc).

All the stellar and kinematic distances presented in this paper are determined following the basic methods together with the adopted calibration and rotation curve presented in Russeil (2003).

### 3.3. The $-42 \text{ km s}^{-1}$ regions

We separate these two HII regions from the next  $-52 \text{ km s}^{-1}$  complex because of their slightly higher velocity and their more evolved appearance.

#### RCW104

This extended region is a Wolf-Rayet bubble with numerous filaments. In [OIII] the aspect is different, a ring is observed (Chu & Treffers 1981) in the inner side of the  $H\alpha$  emission zone. This multi-shell of matter around the star illustrates the different evolutionary phases of the star. The ejected winds from the star created the central cavity interacting with the ejecta. In parallel, Goudis et al. (1988) found some knots with very large velocity within the filaments ( $V_{\text{hel}}$  between  $-100$  and  $-170 \text{ km s}^{-1}$ ). In  $H\alpha$  we observed RCW104 with the Fabry-Perot with both orders 796 and 2604. Some profiles show a splitting allowing us to estimate an expansion velocity of  $20.5$  to  $30.7 \text{ km s}^{-1}$  which is in good agreement with the expansion velocity gave by Chu (1982). Along the brightest filament, large  $H\alpha$  profiles are noted with velocities becoming slightly more negative while going to the East (Fig. 3a). This velocity gradient suggests an expansion toward the East hence a smaller interstellar medium density in this direction. The radio source G332.783-1.445 coincides with the brightest filament and shows a similar velocity of  $-41 \text{ km s}^{-1}$  as for the  $H\alpha$  measurement. The exciting star is the Wolf-Rayet star HD 147419 (WR75). Several authors give 3 kpc for its distance (Chu & Treffers 1981; Goudis et al. 1988; Van der Hutch 1988), while more recently Van der Hutch (2001) estimates its distance at 2.2 kpc.

#### RCW103

RCW103 is a young supernova remnant with a quasi-circular morphology ( $9'$ ) and an associated X-ray source (Gotthelf & Vasisht 1997). Nugent et al. (1984) estimate it is 1000 years old, in agreement with its large velocity dispersion ( $900 \text{ km s}^{-1}$ , Tuohy et al. 1979), and the coincidence between optical filaments and a radio shell. Caswell & Haynes (1975) used HI absorption lines to deduce a distance of 3.3 kpc. Observed with Fabry-Perot order 796, the profile integrated over the brightest part of RCW103 can be fitted with a Gaussian with  $FWMH$  of  $192 \text{ km s}^{-1}$  at the velocity of  $-43 \text{ km s}^{-1}$ . Even if the precision is not good, the estimated velocity is in agreement with the CO velocity ( $-46 \text{ km s}^{-1}$ ).

### 3.4. The $-52 \text{ km s}^{-1}$ complex

Here we provide a detailed analysis of regions with optical counterparts only.

#### RCW 106

In  $H\alpha$  imaging, RCW106 is composed of two distinct structures, noted in the following as RCW106A and RCW106B (Fig. 3c), centred on  $16\text{h}21\text{m}40\text{s}$ ,  $-50^\circ45'$  and  $16\text{h}20\text{m}$ ,  $-50^\circ52'$  respectively. They appear as groups of patches and

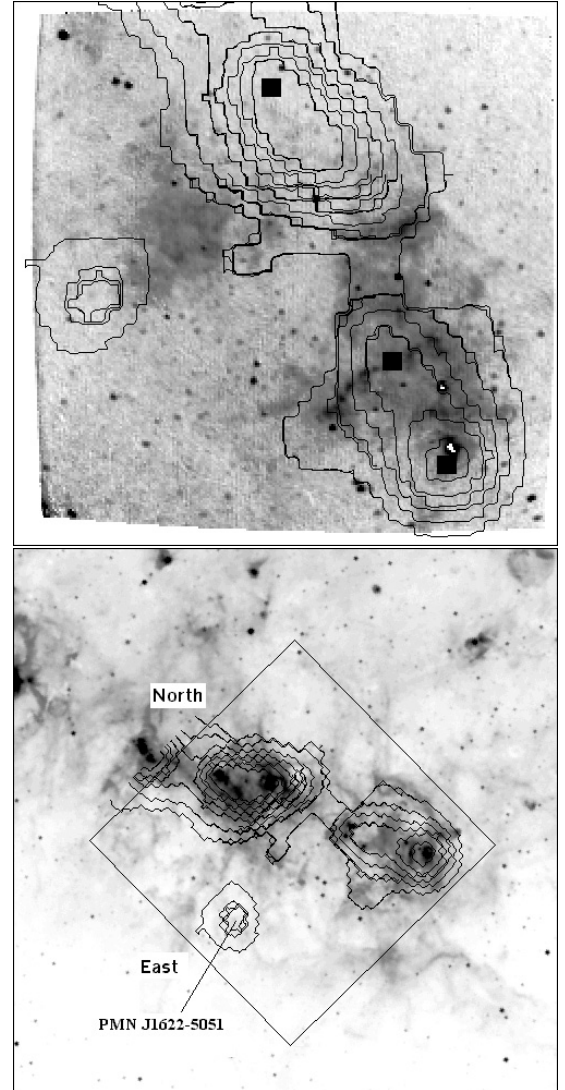


**Fig. 2.** *Top:*  $H\alpha$  image of RCW106 (North is up, East is to the left) overlaid with 5 GHz radio continuum isocontours. The square symbols indicate the position (from north to south) of the radio sources G333.114-0.441, G332.789-0.564 and G332.662-0.607. *Bottom:* MSX greyscale image overlaid with the same 5 GHz radio continuum isocontours (the square delineates the  $H\alpha$  field).

filaments. As underlined by Karnik et al. (2001), the star-formation in RCW106 occurs along a narrow ridge roughly parallel to the galactic plane. In particular, RCW106 takes in three main radio sources (G333.114-0.441, G332.789-0.564 and G332.662-0.607) each of them being able to contribute to the  $H\alpha$  emission and to the complicated  $H\alpha$  velocity field.

To investigate the character of RCW106 we combine mid-infrared Midcourse Space Experiment (MSX) band A data (Price et al. 2001), radio continuum data (GB6 survey, Condon et al. 1993) and our Fabry-Perot  $H\alpha$  data (Fig. 2). The MSX band A ( $\lambda = 8.28 \mu\text{m}$  at 20 arcsec resolution) spans a wavelength range of  $6.8\text{--}10.8 \mu\text{m}$ , which includes emission bands attributed to Polycyclic Aromatic Hydrocarbons (PAH) and thermal emission of dust (Cohen & Green 2001). In the star-forming regions PAH emission is a good tracer of the photon-dominated regions (Leger & Puget 1984). In our

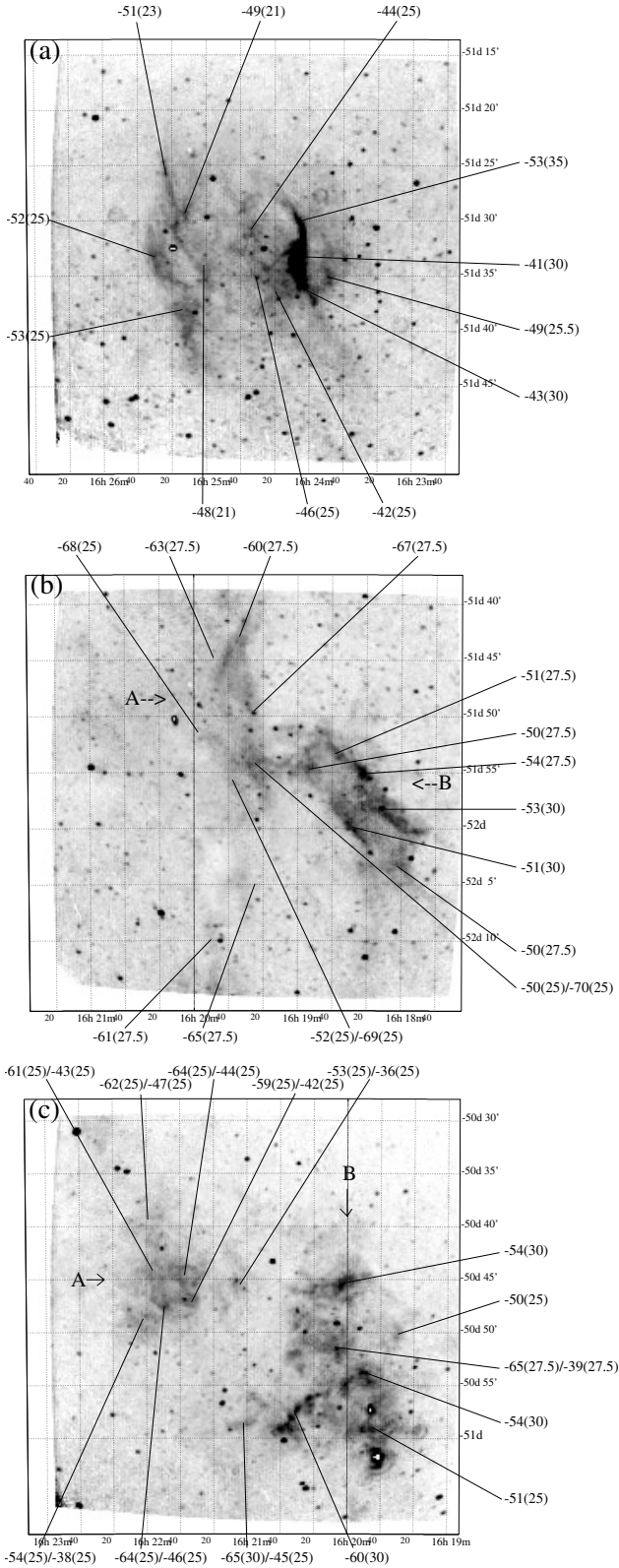


**Fig. 3.** H $\alpha$  image of RCW104, RCW102 and RCW106. For some strategic positions, the  $V_{\text{lsr}}$ , with the line widths in parentheses, are indicated (in  $\text{km s}^{-1}$ ).

framework the photon dominated region allows us to establish the location of the parental molecular cloud and the HII region extension.

The positional coincidence, morphology and relative strengths of the multi-wavelength radio, MIR and H $\alpha$  emission seen towards RCW106B implies that they are all physically related. We can underline the similar extension of the MIR and radio emission. These emissions extend to the North-East from a local maximum centered on G332.667-0.607 suggesting their association. In addition, this morphology suggest that the parental molecular cloud is located South-West of G332.667-0.607. The H $\alpha$  emission does not exactly fit the radio isocontours, especially a faint H $\alpha$  emission is noted in the direction of G332.667-0.607 while this source is intense in MIR and radio. This suggests inhomogeneous local absorption but little external absorption towards the source.

Most of the profiles from RCW106B can be fitted, with only one component with a velocity between  $-51.1$  (in the direction of G332.662-0.607) and  $-60 \text{ km s}^{-1}$  ( $FWHM$   $30 \text{ km s}^{-1}$ ) except at 16h20m05s,  $-50^\circ 52'$  which is a relatively central position of this structure (Fig. 3), where a large increase in profile width can be decomposed into two components at  $-39$  and  $-65 \text{ km s}^{-1}$ . For G332.662-0.607 we adopt an optical velocity of  $-51 \text{ km s}^{-1}$  which is in good agreement with radio and CO velocities ( $V_{\text{H109}\alpha} = -48 \text{ km s}^{-1}$ ,  $V_{\text{CO}} = -52 \text{ km s}^{-1}$ ).

In the direction of G332.789-0.564 we detect H $\alpha$  emission at  $-54 \text{ km s}^{-1}$ . We adopt this velocity for G332.789-0.564 but a definitive association is not possible due to the large contamination by H $\alpha$  emission from G332.662-0.607.

By comparison RCW106A has no obvious radio, FIR or MIR counterpart although in the MSX image a cometary shaped halo is seen pointing toward the radio source G333.114-0.441. A faint extended radio source (PMN J1622-5051) with an IRAS counterpart (IRAS 16186-5044) is seen 8.2 arcmin to the south (PA  $125.3^\circ$ ). For some profiles across RCW106A one component at  $-56 \text{ km s}^{-1}$  is adequate but with a width ( $\sim 37.5 \text{ km s}^{-1}$ ) which is larger than the usual thermal width. Conversely, the asymmetry of other profiles can be well fit via decomposition into two components at  $-59.6$  and  $-42.3 \text{ km s}^{-1}$ ; the most negative component being the most intense. Integrated over RCW106A the profile gives components at  $-57.5 \text{ km s}^{-1}$  and  $-33.6 \text{ km s}^{-1}$ . Assuming the asymmetry is due to expansion motion, the second component betrays gas moving away by about  $24 \text{ km s}^{-1}$ . The projected position of the radio and MSX emission relative to RCW106A and its gas motion suggests they could be linked.

Finally, G333.114-0.441 appears as a bright radio continuum source and an important site of star formation on the MSX image. No H $\alpha$  counterpart is noted, suggesting high absorption in this direction. In Karnik et al. (2001), we can note that G333.114-0.441 and G332.662-0.607 correspond to FIR extended emission and sources with and infrared excess  $\text{IRE} < 1$ , interpretable as a sign of evolved HII regions while G332.789-0.564 corresponds to a more compact source ( $\text{IRE} \approx 1$ ).

To summarize:

- 1) RCW106B is probably the optical counterpart of G332.662-0.607.

- 2) It is not possible to associate unambiguously  $H\alpha$  emission to G332.789-0.564.
- 3) RCW106A can be linked to PMN J1622-5051.
- 4) G333.114-0.441 is probably located behind its parental molecular layer preventing its optical detection.

The stellar distance of RCW106 is poorly known. One possible exciting star has been identified by Georgelin (1976) in projection onto the  $H\alpha$  emission of RCW106: LS3548, B0.5V,  $d = 4.6$  kpc,  $A_v = 2.06$  mag.

#### G331.360+0.507

This source falls just outside (on the West side) of our mapped region. However it is detected on the AAO/UKST  $H\alpha$  image in survey field HA289 (exposure HA18468 see Fig. 4.1) as a large, faint and patchy emission region of approximately circular morphology ( $\sim 6.3'$  diameter). The optical diameter is in very good agreement with the  $6'$  radio diameter (Caswell & Haynes 1987). This optical counterpart and its radio velocities confirms that it belongs to the  $-52$  km s $^{-1}$  complex.

#### G332.148-0.446 and G332.541-0.111

The radio source G332.148-0.446 presents a small  $H\alpha$  emission extension (about  $3' \times 3'$ ) composed of two structures exhibiting the same velocity, the southern part being compact and the northern one more extended. The  $-55$  km s $^{-1}$  ( $FMHW = 30$  km s $^{-1}$ )  $H\alpha$  velocity is identical to that for H109 $\alpha$ . The radio source G332.541-0.111 is small ( $1.5' \times 1.5'$ ) and has an ionized gas velocity of  $-50$  km s $^{-1}$ . On the AAO/UKST  $H\alpha$  image (Figs. 4.4 and 4.5) these two regions clearly show a bright emission patch intersected with extinction lanes together with more extended emission. These two regions exhibit good coincidence between the  $H\alpha$  emission and that in the mid-infrared and the radio.

#### G332.978+0.792 and G333.251+0.006

These sources, not covered by our survey, are well seen on the AAO/UKST  $H\alpha$  image (Figs. 4.6 and 4.7). As the preceding regions G332.978+0.792 presents a typical morphology of an HII region blowing out its parental cloud: a bright patch with dust lanes and a more diffuse extended emission. Due to its evident  $H\alpha$  counterpart and its radio velocity, it is evident to link it to the  $-52$  km s $^{-1}$  layer. G333.251+0.006, an ultra-compact HII region (Bronfman et al. 2000), appears as a very small patch on the  $H\alpha$  image; this optical counterpart confirms its belonging to the  $-52$  km s $^{-1}$  complex.

#### RCW102 and the 16h19m, $-52^\circ 30'$ field

This HII region (Fig. 3b) exhibits two distinct kinematic structures. The first one (named RCW102A) and centered around 16h19m30s,  $-51^\circ 42'$ , has a mean velocity of  $-64$  km s $^{-1}$ . The second one (named RCW102B) is centered around 16h18m30s,  $-51^\circ 57'$  and has a mean velocity of  $-52$  km s $^{-1}$ . The velocity field of RCW102B is relatively constant, while that for RCW102A exhibits a velocity range from  $-60$  to  $-68$  km s $^{-1}$ . The question then arises as to whether these two entities are physically linked.

On examining the variation of profile shape through these structures, we note an abrupt velocity change in these profiles at 16h19m20s,  $-51^\circ 55'$  (location of the apparent superposition of both structures), the transition being marked by the largest profile ( $45$  km s $^{-1}$ ) imposing a 2 component

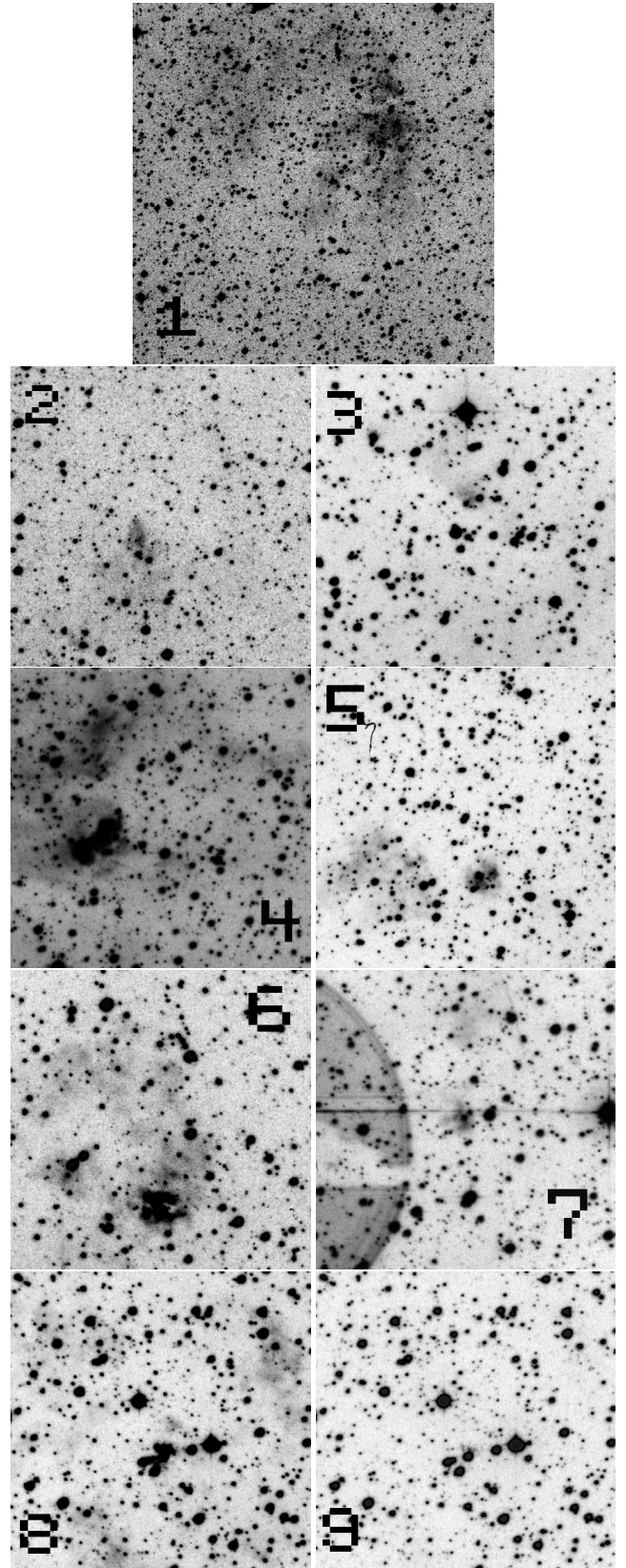


**Fig. 4.** AAO/UKST  $H\alpha$  survey images (North is up, East is left). The first image is a  $12'$  view of G331.36+0.507, others are  $5'$  views of 2 = G331.354+1.07, 3 = G333.726+0.366, 4 = G332.148-0.446, 5 = G332.541-0.111, 6 = G332.978+0.792, 7 = G333.251+0.006 and 8 = G333.61-0.208. The image 9 is the AAO/UKST short red image of G333.61-0.208.

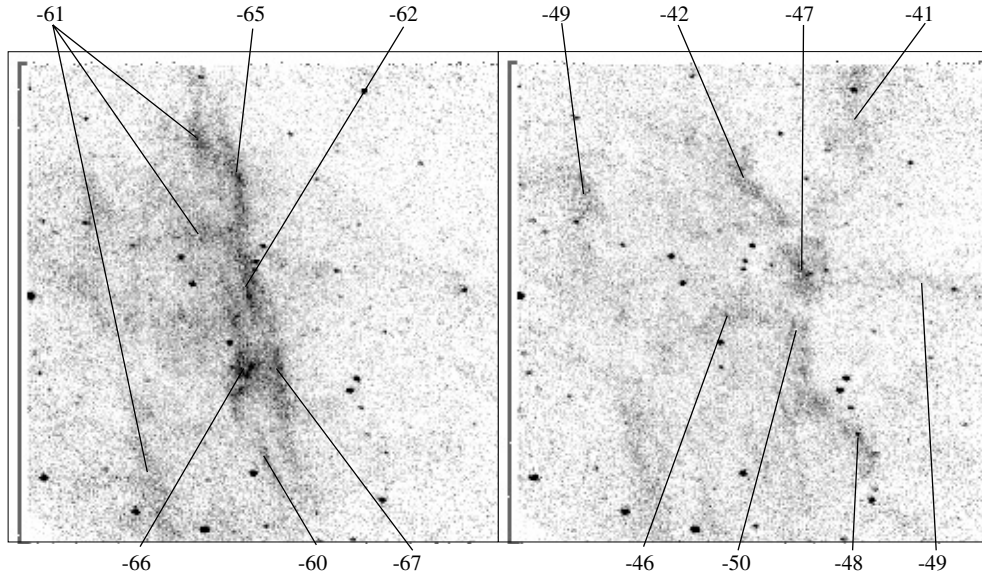


**Fig. 5.** H $\alpha$   $\lambda$ -maps centered at 16h19m,  $-52^{\circ}30'$  at velocity  $-62 \text{ km s}^{-1}$  (left) and  $-46 \text{ km s}^{-1}$  (right). The equivalent bandwidth is  $0.1 \text{ \AA}$ .

decomposition. Moreover, the CO profiles observed in this same direction have no line more negative than  $-52 \text{ km s}^{-1}$ . In addition RCW102B exhibits a radio counterpart (PMNJ1618-5156) and encompass an IRAS point source (IRAS 16148-5150), suggesting it has its own source of excitation. Moreover the extended radio emission matches that for H $\alpha$ . This implies that RCW102A and RCW102B are in fact two distinct layers.

We attempted to find the exciting star(s) of RCW102B. From the Simbad database LS3539 (O6III $n$ , Drilling & Perry 1981) is the only early type star in the direction of the region. For this star we determine  $d = 4.8 \text{ kpc}$  and  $A_v = 3.27 \text{ mag}$ .

Similar kinematical behaviour is observed for a more southerly field at (16h19m,  $-52^{\circ}30'$ ). It also exhibits two structures with different velocities (Fig. 5). The first structure has a rectilinear morphology and appears aligned with RCW102A, while the second, centered at 16h18m39s,  $-52^{\circ}28'$ , exhibits a central clump of H $\alpha$  emission from where five radial extensions emerge. These two structures exhibit mean velocities of  $-62$  and  $-46 \text{ km s}^{-1}$  respectively, in agreement with the values measured from RCW102A and RCW102B. They seem kinematically disconnected because no continuous deformation of the profiles morphology is observed while going from one structure to the other.

To help reveal the nature of these emissions we obtained CO observations towards strategic positions in the region (Figs. 6 and 7). The CO profiles show two distinct features. The first is a line showing a velocity variation from  $-63 \text{ km s}^{-1}$  at P1 to  $-68 \text{ km s}^{-1}$  at P6, reaching a velocity of  $-71 \text{ km s}^{-1}$  at P4. The P4 position corresponds to the main H $\alpha$  filament. The intensity maximum is reached in P3 corresponding to the direction of an H $\alpha$  patch at the same velocity ( $-66 \text{ km s}^{-1}$ ). No line at these velocities is detected in P1 and P6 suggesting the structure is spatially narrow. The velocity variation and the small spatial extent as well as the H $\alpha$  velocity and morphology agreement suggest it looks like a wave moving in the interstellar medium inducing compression along a filament like structure.

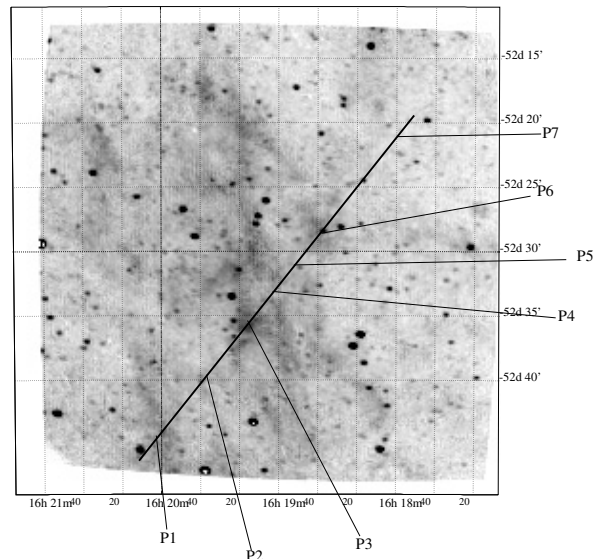


**Fig. 6.** Total H $\alpha$  emission centered at 16h19m,  $-52^{\circ}30'$ . The positions P1 to P7 for which CO profiles have been observed are indicated.

Concerning the second component, in P1 and P7 it appears as a single line at  $-43 \text{ km s}^{-1}$ , while from P2 to P4 it exhibits a larger width and in P5 and P6 it is split into two components at  $-42 \text{ km s}^{-1}$  and  $-51 \text{ km s}^{-1}$ . This splitting can be interpreted as the intersection of the line of sight with the two faces of a local molecular cavity with a mean velocity of  $-46.5 \text{ km s}^{-1}$  (in good agreement with the H $\alpha$  velocity of the 16h18m39s,  $-52^{\circ}28'$  structure) and expansion velocity of  $4.5 \text{ km s}^{-1}$ . Moreover, the drastic change of the relative intensity of the two components in P5 and P6 suggests the medium is highly inhomogeneous which is also underlined by the H $\alpha$  emission.

Filamentary structures are also observed in the southern part of our H $\alpha$  mosaic, their mean velocity being  $-62 \text{ km s}^{-1}$ . These filaments are also seen in the MSX Band A image.

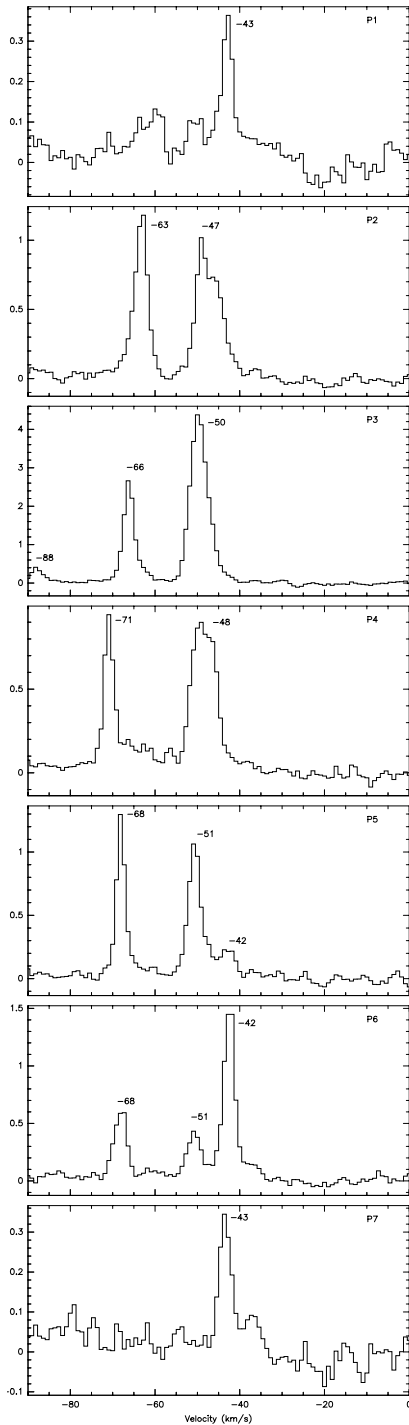


**Fig. 7.** 12CO(2–1) profiles towards the positions P1 to P7.

In this view, the  $-52 \text{ km s}^{-1}$  structures (RCW102B and the 16h18m39s,  $-52^{\circ}28'$  structure) can be directly linked to the star-forming complex, while the  $-63 \text{ km s}^{-1}$  features are superimposed filaments, probably supernovae remnants.

This hypothesis is reinforced by Duncan et al. (1995) who detect, at 2.4 GHz, semi-circular segments which could trace a large  $2^{\circ}$  bubble centered at 332–3.2 (see their Fig. 6).

#### G333.61-0.208 and G333.6-0.1

G333.61-0.208 radio source is one of the brightest infrared source in the sky. Beklin et al. (1973) explain its infrared

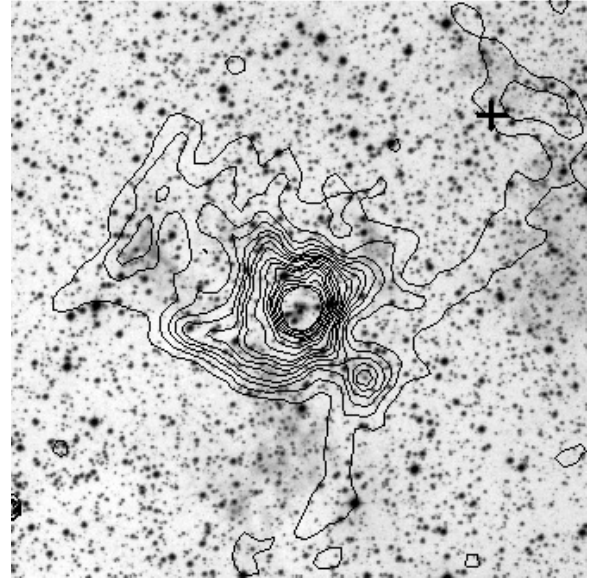


**Fig. 8.** H $\alpha$  image ( $15' \times 15'$ ) of G333.61-0.208 (North is up, East is left) overlaid with MSX band A isocontours. The cross indicates the position of the source G333.6-0.1.

excess by the thermal emission of dust grains. From comparison of optical and infrared data, Hyland et al. (1980) deduce that its more probable geometry is as a “blister” seen face on and located on the near part of a dense molecular cloud.

Churms et al. (1974) detected it photographically quoting a dimension of  $15 \times 5$  arcsec, barely larger than the pixel size of our own H $\alpha$  data. By comparing the AAO/UKST H $\alpha$  (Fig. 4.8) and short red images (Fig. 4.9) the source is clearly detected and appears as 3 knots aligned over 18 arcsec (PA  $260^{\circ}$ ). The AAO/UKST data of the area reveals also patches of more diffuse emission within 6 arcmin around the source. In our H $\alpha$  data the source is detected but the proximity of a foreground star and its small size make its velocity measurement difficult though we estimate a velocity of  $-37 \text{ km s}^{-1}$ . In parallel, a velocity of  $-46.5 \text{ km s}^{-1}$  is found for the H $\alpha$  patches.

Churms et al. (1974) measured a velocity of  $-40 \pm 5 \text{ km s}^{-1}$  from associated  $140 \text{ \AA/mm}$  optical spectroscopy while Fujiyoshi (1999) gives a H9 $\alpha$  velocity of  $-55 \text{ km s}^{-1}$  towards the peak of radio emission and double-peaked lines with velocities around  $-70$  and  $-30 \text{ km s}^{-1}$  to the south. Huang et al. (1999) decompose the CI line in three components at  $-89$ ,  $-48$  and  $-35 \text{ km s}^{-1}$ . The  $-48 \text{ km s}^{-1}$  component is the most intense hence certainly associated to G333.61-0.208. Other components belong either to other ionized regions present along the line of sight or associated with the ambient photodissociation regions of the prominent H II region.

On the MSX band A image (Fig. 8) G333.61-0.208 exhibits a compact emission with 2.4 arcmin radius from where extend filamentary structures up to  $9.5'$ . The H $\alpha$  patches coincide to or complement this extended MIR emission. In addition G333.6-0.1 is superimposed to North-West MIR extension.

There is then strong evidence that the H $\alpha$  patches are linked to G333.61-0.208 and G333.6-0.1. This suggest that the most probable optical velocity is  $-46 \text{ km s}^{-1}$  in good agreement with CO velocity of  $-51 \text{ km s}^{-1}$ . These velocities and the

optical counterparts confirm their belonging to the  $-52 \text{ km s}^{-1}$  complex.

### 3.5. The $-33 \text{ km s}^{-1}$ region

#### G333.726+0.366

This source, not covered by our survey, appears as a faint and extended patch on the AAO/UKST H $\alpha$  image (Fig. 4.3). From a high resolution optical spectrum a  $V_{\text{lsr}}$  velocity of  $-35.5 \pm 3.3 \text{ km s}^{-1}$  is obtained from [NII] and H $\alpha$  lines (Parker, private communication). This measurement and its optical detection make us to choose the near distance.

## 4. Distance of stellar tracers

To complete the gas analysis, we have collected (mainly from the CDS database) all catalogues young hot stars (O to B3) located in a zone of  $4^\circ$  centred at 16h14,  $-51^\circ$ . Distances have been calculated for stars with spectro-photometric measurements (Spectral type,  $U, B, V$  and H $\beta$  photometry). The distance calculation, adopted calibration and distance uncertainties are discussed further in Russeil (2003). Figure 9 shows the resulting histogram of the stellar distance. Two main features are found at 1.8 kpc and 4.2 kpc. Already, two “layers” of stars at similar distances were noted by Westerlund & Elsasser (1981) (at 1.8 and 3.9 kpc) and Muzzio (1974) (at 1.5 and 4 kpc) obtained from zones centered at  $l = 332^\circ, b = -1^\circ$  and  $l = 332^\circ, b = -2^\circ$  respectively. A third narrow feature is noted at 3.2 kpc. In addition features can be noted around 5.3 and 6.9 kpc, but, since only a few stars are available their reliability is less significant.

In parallel, we collected young stellar clusters from Lynga (1987): Pismis 22 (1 kpc), Lynga 6 (1.6 kpc), Ruprecht 118 (1343 pc), Ruprecht 119 (956 pc), NGC 6031 (1823 pc), NGC 6067 (1417 pc), Ruprecht 115 (2160 pc) and Pismis 23 (2.6 kpc). Their mean distance (1.6 kpc) is in agreement with the closest star layer.

## 5. Discussion

We have performed a multispectral study around the  $l = 332^\circ$  direction of the galactic plane to establish the locations of the different star-forming complexes present along the line of sight. This line of sight is of considerable interest as it cuts across three galactic spiral arms: Sagittarius-Carina, Scutum-Crux and Norma. Table 1 summarises the velocity information determined for the various sources detected together with their grouping into complexes based on their spatial and kinematic agreement. The general overview of the area shows very patchy and filamentary H $\alpha$  emission as well as very inhomogeneous absorption (e.g. in the direction of RCW106).

The first layer consists of diffuse emission at  $-5 \text{ km s}^{-1}$ . This velocity is in good agreement with absorption line velocities detected toward the stars of the Upper-Centaurus-Lupus substructure of the Sco-Cen association (Crawford 1991).

On this basis we can confidently link this layer to the Sco-Cen association whose centre is at 170 pc from the Sun (Bochkarev 1987).

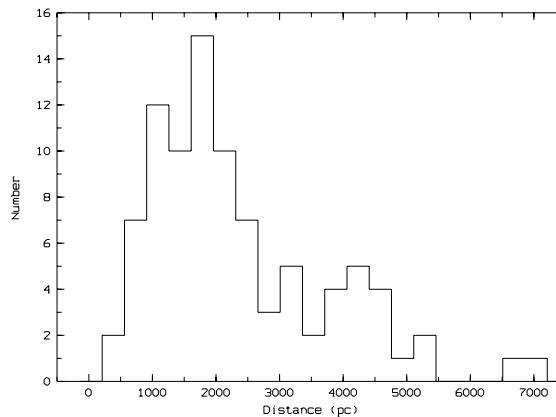


Fig. 9. Number of star per 350 pc bins versus distance.

The second layer of interstellar matter consists of diffuse emission at  $-24 \text{ km s}^{-1}$ . The RCW105 group (at  $V_{\text{lsr}} = -24 \text{ km s}^{-1}$ ) can be directly linked to this layer due to identical velocity. On this basis the distance of this layer can be deduced from the distance of RCW105 itself (1.9 kpc) and the distance to the nearest star layer and clusters (see paragraph 4). This layer is also seen in the two adjacent regions where it consists of diffuse emission which extends across the entire field with the same intensity but is also associated with bright discrete HII regions. In the  $l = 328^\circ$  and  $l = 338^\circ$  directions this emission is detected at  $-20 \text{ km s}^{-1}$  and  $-22 \text{ km s}^{-1}$  respectively. Associated with the Sagittarius-Carina arm its distance is estimated at 1 kpc, 1.9 kpc and 1.4 kpc for the  $l = 328^\circ, 332^\circ$  and  $l = 338^\circ$  directions. The expected distance for a logarithmic spiral structure is between 700 and 950 pc in this longitude range (Russeil 2003) so clear departures from a logarithmic spiral pattern are indicated.

Apart from these two extensive layers which are detected all over the studied region, the next set of complexes, their extents and distances, requires a more precise multi-wavelength approach. Consequently we have analysed the CO latitude-velocity plots of Bronfman et al. (1989). From longitude  $330^\circ$  to  $336^\circ$  CO emission reveals two main layers between  $-110$  and  $-80 \text{ km s}^{-1}$  and between  $-60$  to  $-40 \text{ km s}^{-1}$  though substructures can also be extracted (Table 2). In Table 2 the first two molecular clouds are the most intense structure while the next CO features are at least half as intense as the former. We associate molecular clouds with our complexes on the basis of the correspondence in galactic coordinates and in velocities. We used the rough estimate of the size of the molecular cloud to have an indication of the distance. Indeed, the giant molecular cloud size is between 20 and 100 pc (e.g. Sanders et al. 1985). Hence for a typical  $100 \times 50 \text{ pc}$  cloud, angular sizes are  $1.9^\circ \times 0.95^\circ, 1.4^\circ \times 0.7^\circ, 1.1^\circ \times 0.6^\circ$  and  $0.5^\circ \times 0.3^\circ$  respectively at 3, 4, 5 and 11 kpc. These apparent molecular cloud sizes help us to choose between the near and far kinematic distance for not optically detected complexes. In parallel, the discussed area corresponds to high opacity zone (Feitzinger & Stuewe 1986) with visible extinction between 2.7 and 4.8 mag. In particular from Fig. 1 of Feitzinger & Stuewe (1986) we note the presence of a high opacity zone ( $A_v$  between 4.1 and 4.8 mag) between longitudes  $329^\circ$  and  $335.5^\circ$  and latitudes  $0^\circ$  and  $5^\circ$ .

**Table 2.** The molecular clouds.

	longitude range $\delta l$ °	latitude range $\delta b$ °	Velocity range $\delta v$ km s <sup>-1</sup>
CO cloud I	332.5–334	-0.75–0	-45–-60
CO cloud II	330.625–331.375	-0.75–-0.25	-60–-70
CO cloud III	331–332.5	-0.5–+0.25	-85–-100
CO cloud IV	331.25	+0.5–+0.75	-45–-50
CO cloud V	331.25	+0.8–+1.5	-75–-85
CO cloud VI	331.875–332	-0.25–+0.25	-50–-55
CO cloud VII	331.875–332	+0.5–+0.75	-37–-45
CO cloud VIII	333	+0.25–+1.25	-50–-55
CO cloud IX	333.25	+0.25–+0.75	-60–-65
CO cloud X	334–335.5	0–+0.75	-55–-65
CO cloud XI	333.75–333.625	+0.25–+0.5	-30–-35
CO cloud XII	334.5–334.625	-0.25–+0.125	-30–-35
CO cloud XIII	333.125–334.75	-0.5–+0.5	-80–-90
CO cloud XIV	333.75–335.5	+0.5–+0.8	-60–-70
CO cloud XV	334.875–335.125	0–+0.3	-65–-75
CO cloud XVI	336	-0.5–-1	-45–-55

The presence of an important absorption feature is also seen in Fig. 6a of Dame et al. (2001). This large extinction can explain why some near sources are not optically detected.

#### The $-52$ km s<sup>-1</sup> complex:

This complex undoubtedly can be associated with Cloud I (size  $\delta l = 1.5^\circ$ ,  $\delta b = 0.75^\circ$ ) which is the most intense molecular substructure. Also, Clouds VI and VIII can be associated with this complex but being mostly smaller and fainter than Cloud I, they can be understood as substructures of Cloud I.

This complex is the major spiral feature detected in this area, it can be associated with the second stellar feature at 4.2 kpc seen on the stellar histogram (Fig. 9) which agrees with the distance estimate of RCW102B and RCW106. The stellar distance is very different from the kinematic distance ( $D_{\text{kin}} = 3.5$  kpc).

The stellar distance suggests this complex is in the near side of the Norma arm, but, it is also possible that it belongs in the near side of the Scutum-Crux arm. Indeed, on the one hand, its velocity difference with other complexes in the Scutum-Crux arm, the  $-42$  km s<sup>-1</sup> layer, is not too large and on the other hand we note its velocity difference with the  $-65$  km s<sup>-1</sup> complex which is at 4.2 kpc.

Hence, the  $-52$  km s<sup>-1</sup> complex might belong to the Scutum-Crux arm and exhibits a velocity departure. This fact is favoured by the CO emission (at other longitudes) in the Scutum-Crux arm shows cavities and runaway clouds (e.g. Nyman et al. 1987) that would imply an especially large velocity dispersion for complexes within the Scutum-Crux arm.

#### The $-65$ km s<sup>-1</sup> complex:

CO Cloud II (size  $\delta l = 0.75^\circ$ ,  $\delta b = 0.5^\circ$ ), which is the second most intense feature, can be associated with the  $-65$  km s<sup>-1</sup> complex (Table 1) since the longitude, latitude and velocity ranges are in good agreement. The distance determination for this complex is difficult. Some arguments are in favour of the far distance (non-detection in H $\alpha$  and smaller size than over

complexes) while the lack of absorption features at more negative velocity favours the near distance. This last argument is quite strong because of the presence of the  $-87$  km s<sup>-1</sup> complex in the line of sight which should be seen in absorption if the  $-65$  km s<sup>-1</sup> complex were at the far distance. Then, the near distance ( $D_{\text{kin}} = 4.2$  kpc) is adopted for this complex.

#### The $-87$ km s<sup>-1</sup> complex:

CO Cloud III (size  $\delta l = 1.5^\circ$ ,  $\delta b = 0.75^\circ$ ) can be linked to the  $-87$  km s<sup>-1</sup> complex. Due to no absorption line detected at more negative velocity, the near distance is favoured ( $D_{\text{kin}} = 5.3$  kpc). The near distance choice is consolidated by the HI profiles observed in the direction of G331.026-0.152, G331.259-0.186, G331.353-0.013 and G331.517-0.069 shown by Dickey et al. (2003). These profiles show no absorption to velocities beyond the velocity of the complex. The non-optical detection of this complex can be partly attributed to the Ultra-Compact nature of most of the sources (Bronfman et al. 2000).

#### G331.354+1.07:

G331.354+1.07 can be associated with cloud V. This cloud appears as a small and quite isolated cloud. Its presence confirms our choice not to include G331.354+1.07 in the  $-87$  km s<sup>-1</sup> complex. In addition G331.354+1.07 is optically detected (Fig. 4.2), meaning it is certainly at the near distance ( $D_{\text{kin}} = 4.9$  kpc).

#### The $-91$ km s<sup>-1</sup> complex:

We can assign the  $-91$  km s<sup>-1</sup> complex to cloud XIII (size  $\delta l = 1.6^\circ$ ,  $\delta b = 1^\circ$ ). Due to no more negative absorption lines evident in this complex it can be put at its near distance ( $D_{\text{kin}} = 5.5$  kpc). The near distance choice is conformed by the large latitude extension for the complex.

#### The $-42$ km s<sup>-1</sup> layer:

On Bronfman et al. plots (1989) diffuse CO emission with velocity between  $-37$  km s<sup>-1</sup> and  $-45$  km s<sup>-1</sup> is noted at every longitude, encompassing cloud IV. Its maximum latitude range is  $-1^\circ$  to  $+0.75^\circ$ . It has similar velocity as the  $-42$  km s<sup>-1</sup> diffuse layer. This layer ( $D_{\text{kin}} = 3$  kpc) can be associated with the stellar feature at 3.2 kpc (see Fig. 9) and the HII regions at  $-42$  km s<sup>-1</sup>. This lies in the near section of the Scutum-Crux arm. Already, a  $-40$  km s<sup>-1</sup> layer is observed in the two adjacent regions which were placed at 2.3 kpc ( $l = 328^\circ$ ) and 3 kpc ( $l = 338^\circ$ ) with agreement between the stellar and kinematic distances.

#### G333.726+0.366 and G334.684-0.107:

These two sources have identical velocity but are not at the same distance. G333.726+0.366 can be associated with the small cloud XI. Due to its optical detection, it is placed at the near distance ( $D_{\text{kin}} = 2.5$  kpc). G334.684-0.107 can be associated with the small cloud XII. It is not optically detected, hence it is put at the far distance ( $D_{\text{kin}} = 12.8$  kpc).

#### The $-73$ km s<sup>-1</sup> complex and G335.978+0.18 :

As in the case above, these two entities have similar velocity but seem to be at different distances. Cloud XIV (size  $\delta l = 1.75^\circ$ ,  $\delta b = 0.3^\circ$ ) can be linked to the  $-73$  km s<sup>-1</sup> complex while G335.978+0.18 is linked to cloud XV. On the basis of the absorption lines, the  $-73$  km s<sup>-1</sup> complex is placed at the far distance ( $D_{\text{kin}} = 10.7$  kpc) while G335.978+0.18 ( $-78$  km s<sup>-1</sup>) is placed at the near distance ( $D_{\text{kin}} = 4.9$  kpc).

**G334.714-0.665:**

For this source no CO counterpart in Bronfman et al. (1989) is found. Due to its positive velocity, it is unambiguously placed at the far distance ( $D_{\text{kin}} = 17.4$  kpc)

**The  $-50$  km s $^{-1}$  complex and G336.022-0.819 :**

G336.022-0.819 can be associated with cloud XVI. This cloud appears small and quite isolated from the  $-50$  km s $^{-1}$  complex. Since it has no optical detection G336.022-0.819 ( $D_{\text{kin}} = 12.1$  kpc) can be put at the far kinematic distance. The most probable molecular counterpart of the  $-50$  km s $^{-1}$  complex is the cloud X (size  $\delta l = 1.5^\circ$ ,  $\delta b = 0.75^\circ$ ). Due to no absorption line at more negative velocity and the similar size of cloud X as cloud I, the  $-50$  km s $^{-1}$  complex ( $D_{\text{kin}} = 3.5$  kpc) can be put at the near distance. But, by continuity with the  $-52$  km s $^{-1}$  complex, we must adopt the same stellar distance (4.2 kpc). The sources of this complex are on the line of sight of the bright ionised bubble surrounding RCW107, this makes difficult their optical detection.

**6. Conclusion**

We clearly identify the Sagittarius-Carina arm via its intense diffuse emission and the presence of the bright HII region RCW105. This portion of the Sagittarius-Carina arm is well connected to its other parts identified in the  $l = 328^\circ$  and  $l = 338^\circ$  areas. The distance of the arm in this longitude range (between 1 and 1.9 kpc) clearly shows a departure from the logarithmic spiral pattern (where the expected distance is between 700 and 950 pc) which is followed by the arm tracers up to  $l = 283^\circ$  (Russeil 2003).

The other complexes show that the near section of the Norma arm is traced by complexes with velocities between  $-65$  km s $^{-1}$  and  $-91$  km s $^{-1}$  and distances from 4.2 to 5.5 kpc. This arm is traced by complexes at  $-50$  km s $^{-1}$  ( $D_{\text{star}} = 4.4$  kpc) and  $-61$  km s $^{-1}$  ( $D_{\text{star}} = 5$  kpc) in the  $l = 338^\circ$  area and by a complex at  $-73$  km s $^{-1}$  ( $D_{\text{kin}} = 4.6$  kpc) in the  $l = 328^\circ$  area. The Scutum-Crux arm, between  $l = 328^\circ$  and  $l = 338^\circ$ , appears to be traced by two velocity layers: the more diffuse layer around  $-40$  km s $^{-1}$  associated with a few stars and HII regions and the  $-52$  km s $^{-1}$  and  $-50$  km s $^{-1}$  complexes.

Compared to the adjacent regions at  $328^\circ$  and  $338^\circ$  we note the importance of the  $-65$  km s $^{-1}$  extended emission. In the  $l = 338^\circ$  area, discrete HII regions with a velocity around  $-61$  km s $^{-1}$  have been detected in H $\alpha$  while no extended emission at a similar velocity is noted. In the  $l = 328^\circ$  area only a faint H $\alpha$  counterpart of the radio source G327.759-0.351 is detected around  $-65$  km s $^{-1}$ . In the present area, because no discrete HII region can be linked to the  $-65$  km s $^{-1}$  filaments and patches, this emission probably has a different origin from that of a star-forming complex. Duncan et al. (1997) detected a possible Supernova Remnant (SNR) centered at 332.0-3.2 and  $2^\circ$  angular size from radio continuum emission at 2.4 GHz for which the  $-65$  km s $^{-1}$  emission could be a counterpart. In addition, the latitude position and size of this SNR could explain why we detect the  $-65$  km s $^{-1}$  filaments and patches only in the southern part of the mosaic.

**References**

- Amram, P., Boulesteix, J., Georgelin, Y. M., et al. 1991, *The Messenger*, 64, 44
- Becklin, E. E., Frogel, J. A., Neugebauer, G., et al. 1973, *ApJ*, 182, L125
- Bochkarev, N. G. 1987, *Ap&SS*, 138, 229
- Brand, J., Van der Bij, M., de Vries, C., et al. 1984, *A&A*, 139, 181
- Bronfman, L., Alvarez, H., Cohen, R. S., & Thaddeus, P. 1989, *ApJS*, 71, 481
- Bronfman, L., Casassus, S., May, J., et al. 2000, *A&A*, 358, 521
- Caswell, J. L., & Haynes, R. F. 1987, *A&A*, 171, 261
- Caswell, J. L., Murray, J. D., Roger, R. S., et al. 1975, *A&A*, 45, 239
- Chu, Y. H., & Treffers, R. R. 1981, *ApJ*, 250, 615
- Chu, Y. H. 1982, *ApJ*, 254, 578
- Churms, J., Feast, M. W., Glass, I. S., et al. 1974, *MNRAS*, 169, 39
- Cohen, M., & Green, A. J. 2001, *MNRAS*, 325, 531
- Condon, J. J., Griffith, M. R., & Wright, A. E. 1993, *AJ*, 106, 1095
- Crawford, I. A. 1991, *A&A*, 247, 183
- Dame, T. M., Hartmann, D., & Thaddeus, P. 2001, *ApJ*, 547, 792
- Dickey, J., McClure-Griffiths, N., Gaensler, B., et al. 2003, *ApJ*, 585, 801
- Duncan, A., Stewart, R., Haynes, R., et al. 1997, *MNRAS*, 277, 36
- Drilling, J. S., & Perry, C. L. 1981, *A&AS*, 45, 439
- Feitzinger, J. V., & Stuewe, J. A. 1986, *Vistas Astron.*, 29, 291
- Fujiyoshi, T. 1999, in *star formation 1999 Proc.*, 401
- Gardner, F. F., & Whiteoak, J. B. 1984, *MNRAS*, 210, 23
- Georgelin, Y. M., & Georgelin, Y. P. 1976, *A&A*, 49, 57
- Georgelin, Y. M., Amram, P., Georgelin, Y. P., et al. 1994, *A&AS*, 108, 513
- Georgelin, Y. M., Russeil, D., Marcelin, M., et al. 1996, *A&AS*, 120, 41
- Gotthelf, E. V., & Vasisht, G. 1997, *ApJ*, 486, L133
- Goudis, C. D., Meaburn, J., & Whitehead, M. J. 1988, *A&A*, 191, 341
- Huang, M., Bania, T. M., Bolatto, A., et al. 1999, *ApJ*, 517, 282
- Hyland, A. R., McGregor, P. J., Robinson, G., et al. 1980, *ApJ*, 241, 709
- Karnik, A. D., Ghosh, S. K., Rengarajan, T. N., et al. 2001, *MNRAS*, 326, 293
- le Coarer, E., Amram, P., Boulesteix, J., et al. 1992, *A&A*, 257, 389
- Leger, A., & Puget, J. L. 1984, *A&A*, 137, 5
- Lynga, G. 1987, *Catalogue of open cluster data*, distributed by the CDS Strasbourg
- Muzzio, J. C. 1974, *AJ*, 79, 959
- Nugent, J. J., Pravdo, S. H., Garmire, G. P., et al. 1984, *ApJ*, 284, 612
- Nyman, L. A., Thaddeus, P., Bronfman, L., & Cohen, R. S. 1987, *ApJ*, 314, 374
- Otrupcek, R. E., Hartley, M., & Wang, J. 2000, *PASA*, 17, 92
- Paladini, R., Burigana, C., Davies, R. D., et al. 2003, *A&A*, 397, 213
- Parker, Q. A., & Phillipps, S. 2003, in *IAU 8th Asian-Pacific Regional Meeting*, ed. S. Ikeuchi, J. Hearnshaw, & T. Hanawa, Vol. 1, 165
- Price, S. D., Egan, M. P., Carey, S. J., et al. 2001, *AJ*, 121, 2819
- Russeil, D. 2003, *A&A*, 397, 133
- Russeil, D., & Castets, A. 2004, *A&A*, 417, 107
- Sanders, D., Scoville, N., & Solomon, P. 1985, *ApJ*, 289, 373
- Shaver, P. A., McGee, R. X., Newton, L. M., et al. 1983, *MNRAS*, 204, 53
- Tuohy, I. R., Cordova, F. A., Garmire, G. P., et al. 1979, *ApJ*, 230, L27
- Turner, B. E. 1979, *A&AS*, 37, 1
- Van der Hucht, K. A., Hidayat, B., Admiranto, A. G., et al. 1988, *A&A*, 199, 217
- Van der Hucht, K. A. 2001, *NewAR*, 45, 135
- Westerlund, B. E., & Elsasser, H. 1981, *SSRv*, 28, 109
- Whiteoak, J. B., & Gardner, F. F. 1974, *A&A*, 37, 389
- Yamaguchi, R., Saito, H., Mizuno, N., et al. 1999, *PASJ*, 51, 791

# Online Material

**Table 1.**  $V_{\text{lsr}}$  radial velocities of HII region complexes only.

Identification	H $\alpha$ km s $^{-1}$	Radio recomb. km s $^{-1}$	Molecular km s $^{-1}$	Abs km s $^{-1}$	$V_{\text{sys}}$ km s $^{-1}$	$d_{\text{adopted}}$ kpc
330.677-0.396		-61	-66; -4/-47/-58/-67/-81/-96	-66		
330.856-0.371		-56	-63; -63; -62.2	-53/-55/-50; -63; -62; -63 -63/-55/-50		
331.058-0.437			-63.5			
331.1-0.4		-55	-104/-54; -51	-61/-53/-46/-19; -52; -53; -55/-42		
331.110-0.506		-68	-66; -51/-64/-94; -66.5	-66; -63/-55/-49	-65 (Near)	4.2
331.169-0.455			-69.4			
331.314-0.336		-64	-42/-65/-86/-99; -64.8	-66/-42/-14; -67		
331.421-0.360			-62.6			
330.286+0.496			-93.5			
330.293-0.394			-80			
330.949-0.174		-90.5	-89; -100/-91/-62/-44; -91; -89.7	-90; -90; -90/-46		
331.026-0.152		-89	-37/-45/-53/-66/-82/-92	-92/-47		
331.126-0.239			-87			
331.146+0.134			-75.3		-87 (Near)	5.3
331.259-0.186		-85	-89; -88; -111/-98/-88/-67/-49; -87.7	-89		
331.353-0.013		-81	3/-4/-47/-66/-78/-87/-92/-99	-89/-66/-49		
331.517-0.069		-89	-100.7; -90; -89; -89/-59	-100/-89/-57/-48; -100/-89/-56/-48/-41; -89/-64/-50/-42/-18/0.4		
331.354+1.07	UKST	-79	-78.3		-79 (Near)	4.9
RCW103	-43		-99/-89/-72/-46/-30/-26	-43		
332.783-1.445 (=RCW104)	-41 to -53	-41			-42 (Near)	*3.2
331.360+0.507	UKST	-46	-96/-64/-46/-38/-23	-46/-38		
332.148-0.446	-55	-55	-55.5; -57/-74; -55.7	-57; -56; -57/-43		
332.293-0.095			-48.4			
332.322-0.563			-51.9			
332.541-0.111	-50	-50	-82/-70/-57/-48; -46.7	-49		
332.662-0.607 (=RCW106)	-51	-48	-50; -52; -49.6	-73/-50; -50; -57/-50 -57/-50		
332.789-0.564	-54	-57	-55.7; -55; -59; -57; -107/-57/-49	-59; -59		
332.978+0.792	UKST	-52	-85/-74/-60/-48/-36/-31; -44.5	-48		
333.114-0.441		-52	-54; -54; -51; -52; -51.2	-52; -55/-44/-20 -54/-19	-52 (Near)	*4.2
333.251+0.06	UKST		-46.9			
333.340-0.129			-59.7			
333.469-0.162			-45.3			
333.292-0.371		-50	-52; -52; -107/-52; -49.5	-54/-44/-50/-23; -57 -55/-42; -57		
333.684-0.457		-50	-104/-88/-55/-43/-33/-13/-5	-55; -55/-23; -54 -54/-42/-22; -56		
333.0-0.4			-54; -56; -54; -107/-71/-55			
333.3-0.4		-50.1	-51	-54/-44/-40/-23; -54; -54		
333.0+0.8		-52		-48		
333.0-0.6		-52		-48		
RCW102	-53 to -64		-55			
333.6-0.1	UKST	-54	-88/-71/-51/-40	-87/-44		
333.61-0.208	-46.5	-46	-51; -109/-89/-51/-36	-41; -53/-42; -46/-41 -91/-46/-40/-13; -52/-42		
331.9+2.8			-25			
331.9+2.4			-27			
332.956+1.804 (=RCW105)			-22.2		-24 (Near)	*1.9
333.04+2.02 (=RCW105)	-21.3	-20	3/-8/-32/-35/-59			

**Table 1.** continued.

Identification	H $\alpha$ km s $^{-1}$	Radio recomb. km s $^{-1}$	Molecular km s $^{-1}$	Abs km s $^{-1}$	$V_{\text{sys}}$ km s $^{-1}$	$d_{\text{adopted}}$ kpc
332.769-0.007			-95			
333.168-0.081		-91	-91.8; -12/-47/-62/-69/-87/-101/-105	-89/-47/-19		
333.2-0.1		-91		-89/-47/-19; -88; -87	-91 (Near)	5.5
333.0+0.0				-91		
333.726+0.366	UKST		-33		-33 (Near)	2.5
334.173+0.068		-70	-20/-40/-65/-89/-102	-86/-40	-73 (Far)	10.7
334.529+0.825		-77				
334.684-0.107		-32	-2.5/-33/-44/-88/-112		-33 (Far)	12.8
334.714-0.665		16	11/17/-20/-38/-43/-92/-102		17	17.4
334.330+0.967			-50.4			
335.582-0.284			-46.6			
335.748-0.134		-52		-45	-50 (near)	*4.2
335.751+0.110		-51		-38		
335.978+0.18		-79	-36/-42/-46/-56/-62/-70/-77/-108/-124	-37	-78 (Near)	4.9
336.022-0.819			-48.3		-48 (Far)	12.1